Aalto University

OPEN ACCESS

This is an electronic reprint of the original article.
This reprint may differ from the original in pagination and typographic detail.

Li, Chen; Tian, Ruijuan; Chen, Xiaoqing; Gu, Linpeng; Luo, Zhengdong; Zhang, Qiao; Yi, Ruixuan; Li, Zhiwen; Jiang, Biqiang; Liu, Yan; Castellanos-Gomez, Andres; Chua, Soo Jin; Wang, Xiaomu; Sun, Zhipei; Zhao, Jianlin; Gan, Xuetao

Waveguide-Integrated $MoTe_2$ p- i- n Homojunction Photodetector

Published in:
ACS Nano

DOI:
10.1021/acsnano.2c08549

Published: 27/12/2022

Document Version
Peer-reviewed accepted author manuscript, also known as Final accepted manuscript or Post-print

Please cite the original version:
Li, C., Tian, R., Chen, X., Gu, L., Luo, Z., Zhang, Q., Yi, R., Li, Z., Jiang, B., Liu, Y., Castellanos-Gomez, A., Chua, S. J., Wang, X., Sun, Z., Zhao, J., & Gan, X. (2022). Waveguide-Integrated $MoTe_2$ p- i- n Homojunction Photodetector. *ACS Nano*, *16*(12), 20946-20955. https://doi.org/10.1021/acsnano.2c08549

This material is protected by copyright and other intellectual property rights, and duplication or sale of all or part of any of the repository collections is not permitted, except that material may be duplicated by you for your research use or educational purposes in electronic or print form. You must obtain permission for any other use. Electronic or print copies may not be offered, whether for sale or otherwise to anyone who is not an authorised user.

Waveguide-integrated $MoTe_2$ *p-i-n* Homojunction Photodetector

Chen Li[1], *Ruijuan Tian*[1], *Xiaoqing Chen*[1], *Linpeng Gu*[1], *Zhengdong Luo*[2], *Qiao Zhang*[1], *Ruixuan Yi*[1], *Zhiwen Li*[1], *Biqiang Jiang*[1], *Yan Liu*[2], *Andres Castellanos-Gomez*[3], *Soo Jin Chua*[4,5], *Xiaomu Wang*[6], *Zhipei Sun*[7], *Jianlin Zhao*[1] & *Xuetao Gan*[1,*]

[1] Key Laboratory of Light Field Manipulation and Information Acquisition, Ministry of Industry and Information Technology, and Shaanxi Key Laboratory of Optical Information Technology, School of Physical Science and Technology, Northwestern Polytechnical University, Xi'an 710129, China.

[2] Wide Bandgap Semiconductor Technology Disciplines State Key Laboratory, School of Microelectronics, Xidian University, Xi'an 710071, China

[3] Materials Science Factory, Instituto de Ciencia de Materiales de Madrid (ICMM-CSIC), Madrid E-28049, Spain.

[4] Department of Electrical and Computer Engineering, National University of Singapore, 4 Engineering Drive 3, Singapore 117583, Singapore.

[5] LEES Program, Singapore-MIT Alliance for Research & Technology (SMART), 1 CREATE Way, #10-01 CREATE Tower, Singapore 138602, Singapore.

[6] School of Electronic Science and Engineering, Nanjing University, Nanjing 210093, China.

[7] Department of Electronics and Nanoengineering and QTF Centre of Excellence, Aalto University, Aalto FI-00076, Finland.

[*] Email: xuetaogan@nwpu.edu.cn

ABSTRACT: Two-dimensional (2D) materials, featuring unique electronic and optical properties and dangling-bond-free surfaces, are promising for developing high-performance on-chip photodetectors in photonic integrated circuits. However, most of the previously reported devices operating in the photoconductive mode suffer from a high dark current or a low responsivity. Here, we demonstrate a $MoTe_2$ *p-i-n* homojunction fabricated directly on a silicon photonic crystal (PC) waveguide, which enables on-chip photodetection with ultralow dark current, high responsivity, and fast response speed. The adopted silicon PC waveguide is electrically split into two individual back gates to selectively dope the top regions of the $MoTe_2$ channel in *p* or *n* types. High-quality reconfigurable $MoTe_2$ (*p-i-n*, *n-i-p,* *n-i-n*, *p-i-p*) homojunctions are realized successfully, presenting rectification behaviors with ideality factors approaching 1.0 and ultralow dark currents less than 90 pA. Waveguide-assisted $MoTe_2$ absorption promises a sensitive photodetection in the telecommunication O-band from 1260 nm to 1340 nm, though it's close to $MoTe_2$'s absorption band-edge. A competitive photoresponsivity of 0.4 A/W is realized with a light on/off current ratio exceeding 10^4 and a record-high normalized photocurrent-to-dark-current ratio of 10^6 mW^{-1}. The ultrasmall capacitance of *p-i-n* homojunction and high carrier mobility of $MoTe_2$ promise high dynamic response bandwidth close to 34.0 GHz. The proposed device geometry has the advantages of employing silicon PC waveguide as the back-gates to build 2D material *p-i-n* homojunction directly and simultaneously to enhance light–2D material interaction. It opens up a new avenue to develop 2D material-based photodetectors, laser diodes, and electro-optic modulators on silicon photonic chips.

KEYWORDS: $MoTe_2$, two-dimensional materials, *p-i-n* homojunction, lateral junction, photodetector, waveguide-integrated, silicon photonics.

Integrating two-dimensional (2D) materials on silicon photonic structures has been considered as a promising strategy to solve the problem of the absence of telecom-band photodetection in silicon photonics.[1, 2] In previously reported works, several silicon chip-integrated 2D material photodetectors have been realized with the photoconductive mechanism, which is not amenable for reducing the dark current and power consumption, and improving response speed and photodetectivity. For example, a silicon–graphene hybrid waveguide photodetector has been demonstrated with a 3 dB bandwidth exceeding 40 GHz and a high responsivity of ~0.4 A/W at a low bias voltage of –0.3 V. Unfortunately, the device presented a high dark current at the level of mA.[3] In order to overcome the disadvantage of high dark current for graphene-based photodetectors, many works have relied on the photo-thermoelectric (PTE) effect of graphene at zero bias.[4-6] Although the photodetectors based on PTE effect can respond quickly, it's difficult to achieve high responsivity without optical enhancement.[1, 3] The operation at zero bias is unaffected by dark current. But it cannot solve the problem of large dark current fundamentally and the single operation limits the wide application of the device.

In this work, we propose a waveguide-integrated 2D material photodetector operating with the photovoltaic mechanism provided by a *p-i-n* homojunction made from a few-layer $MoTe_2$, which enables ultralow dark current, high responsivity, and fast response speed. It exploits the advantage of 2D materials to effect electron- or hole-doping simply by applying an electrostatic field, which is difficult to be done this way in bulk semiconductors. Figure 1a schematically

displays the structure and operation principle of the proposed device. A silicon photonic crystal (PC) waveguide is employed, which is electrically separated into three sections by two sub-100 nm air-slots in the central waveguide region. The middle part of the three sections is the central line defect of the PC waveguide, where most of the optical guided mode locates. The two side sections beyond the air-slots are the air-hole regions of the PC waveguide, which provide the Bragg reflection to confine the guided mode in the central line defect. The PC waveguide is fabricated on a lightly *p*-doped silicon slab, which is also used for making contacts to electrodes. A thin *h*-BN dielectric film is covered over the silicon PC waveguide to isolate it electrically from the top $MoTe_2$ layer. Electrically, the two side sections of the PC waveguide function as separate back gates (G_1, G_2) to the top $MoTe_2$ channel, which could provide vertical electric fields across the corresponding $MoTe_2$ regions to dope them into *p*- or *n*-type as desired (see Figure 2a). The central region of the $MoTe_2$ channel over the central line defect of the PC waveguide maintains intrinsic (*i*-type) due to the absence of an external electric field. Consequently, a $MoTe_2$ *p*-*i*-*n* homojunction could be constructed over the PC waveguide. The intrinsic region of the $MoTe_2$ *p*-*i*-*n* homojunction couples with the guided mode of the PC waveguide and absorbs optical power from it to effectively generate photocarriers. With a lateral electrical bias across the *p*-*i*-*n* homojunction, the separation of photocarriers is realized to yield a considerable photocurrent.

Chip-integrated 2D material photodetectors employing the vertical or lateral *p*-*n* junctions have been reported.[4, 5, 7-9] Compared with them, the proposed waveguide-integrated $MoTe_2$ lateral *p*-*i*-*n* homojunction has unique advantages. Different from the vertically van der Waals stacked heterogeneous and homogeneous *p*-*n* junctions, the lateral *p*-*i*-*n* homojunction is not only easy to fabricate, but also profitable to form a continuous band alignment across the entire

device, which eliminates the possible defects involved in heterojunction and leads to more efficient rectification characteristics and photovoltaic responses.[10] In addition, with an intrinsic region sandwiched between the *p*- and *n*-type regions, the lateral *p-i-n* homojunction reduces the junction capacitance and turn-off current, increases the photoactive area, and improves the photoelectric conversion efficiency. These characteristics are essential for high-performance photodetection with low dark current, high photoresponsivity, and fast response speed.

In a fabricated device integrated with an 8.2 nm thick few-layer $MoTe_2$, by applying different configurations of gate voltages on the two separated PC back gates (G_1, G_2), reconfigurable (*p-i-n*, *n-i-p*, *n-i-n*, *p-i-p*) $MoTe_2$ homojunctions are achieved with ideality factors close to 1.0. In this arrangement, the high-quality $MoTe_2$ *p-i-n* homojunction promises a competitive photoresponsivity of 0.4 A/W at the wavelength of 1300 nm with an ultralow dark current less than 90 pA, resulting in a record-high normalized photocurrent-to-dark-current ratio exceeding 10^6 mW^{-1}. The *p-i-n* homojunction photodetector is expected to have a large bandwidth of ~34 GHz, though the measured best response time is 2 μs limited by our measurement instrument. The performances are competitive with those achieved in chip-integrated photodetectors based on bulk semiconductors, indicating the great potentials of the waveguide-integrated $MoTe_2$ *p-i-n* homojunction in silicon photonics.

RESULTS AND DISCUSSION

Fabrication and Guided Mode Simulation of PC Waveguide Integrated with $MoTe_2$ *p-i-n* Homojunction. The details of device fabrications are provided in the section of Materials and methods. Briefly, the PC waveguide is fabricated on a 220 nm thick silicon-on-insulator wafer using the techniques of electron beam lithography and inductively coupled plasma etching. As

illustrated in the device cross sectional view in Figure 1b, the mechanically exfoliated *h*-BN and $MoTe_2$ layers are transferred onto the PC waveguide in sequence. The *h*-BN is the dielectric layer for electrically gating the top $MoTe_2$ layer. The drain and source electrodes (D and S) of the $MoTe_2$ channel are then deposited using the transfer-printing technique.[11-16] Finally, the $MoTe_2$ channel is capped by another *h*-BN layer to protect it from environmental degradation. The optical microscope image of the fabricated device is shown in Figure 1c. The electrical isolation air-slots divide the silicon slab into four electrically independent parts to support the electrodes of D, S, G_1, and G_2. The slotted silicon slab could provide a planar platform for the easy transfers of 2D materials and metal electrodes, which simplifies the fabrication process flow and improves device performance without material wrinkles. The $MoTe_2$ channel length between the source and drain contacts is ~8.7 μm. The length of the $MoTe_2$ layer along the PC waveguide is ~12.6 μm, ensuring a long light–$MoTe_2$ interaction. The $MoTe_2$ layer has a thickness of 8.2 nm revealed by the atomic force microscopy (AFM) (see the Supporting Figure S1). Figure 1d shows the scanning electron microscope (SEM) image of the fabricated PC waveguide before the integration of 2D materials. The air-holes of the PC pattern have a lattice constant of 300 nm and a radius of 80 nm. The waveguide is formed by missing one line of air-holes. At the boundary between the air-hole region and the central line-defect, there are two 80 nm wide air-slots, which leave the middle waveguide with a width of 520 nm. The SEM image shows clear air-holes and smooth sidewalls in the PC waveguide.

To study the light propagation and light–$MoTe_2$ interaction in the device, its guided mode is simulated, as shown in Figure 1e (also see the Supporting Figure S2). The top image displays the in-plane electric field distribution of the guided mode in the PC waveguide integrated with the *h*-BN and $MoTe_2$ layers. The 80 nm wide air-slots together with the adjacent PC patterns well

confines the light in the waveguide, as clearly seen in the Supporting Figure S2. The bottom image of Figure 1e gives the cross sectional view of the electric field distribution in the guided mode. The near-field of the guided mode overlaps with the central intrinsic region of the top $MoTe_2$ *p-i-n* homojunction. For the guided light with photon energy larger than the optical bandgap of the few-layer $MoTe_2$, it would be absorbed effectively. The absorption coefficient of the $MoTe_2$ layer on the guided mode is estimated as ~0.53 dB/μm at the wavelength of 1302 nm as obtained from the mode simulations (Supporting Note 4). It is consistent with the experimental measurement of ~0.55 dB/μm. With the assistance of the waveguide, the light–$MoTe_2$ interaction length is extended to give an improved photoresponsivity compared with the free-space illumination configuration.

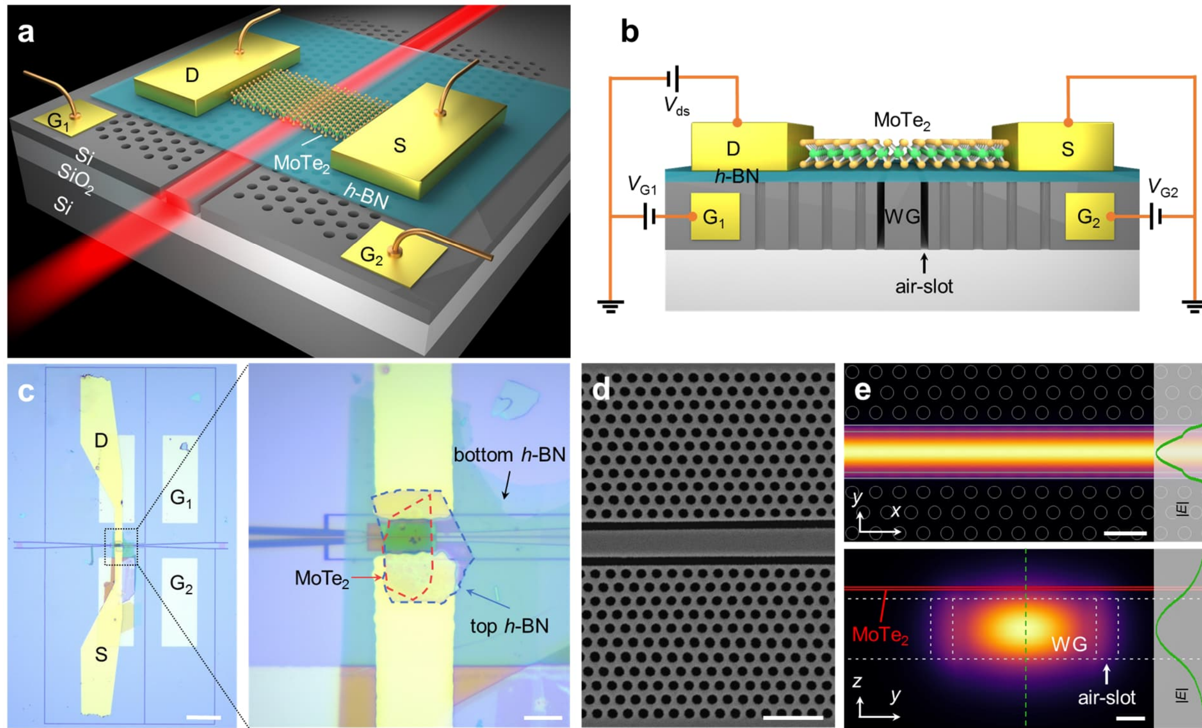

Figure 1. Design of the waveguide-integrated $MoTe_2$ *p-i-n* homojunction photodetector. (a) Schematic of the $MoTe_2$ *p-i-n* homojunction photodetector constructed on a PC waveguide with two air-slots, showing optical mode propagating in the central waveguide and two separated back gates provided by the silicon

PC slab. (b) Schematic cross-section of the device showing the electrical connections. Another view indicating the *p-i-n* homojunction is shown in Figure 2a. (c) Left: Optical microscope image of a fabricated device. Scale bar, 100 µm. Right: Zoomed image of the active section of the device, consisting of a few-layer $MoTe_2$ flake (red dashed line), top (blue dashed line), and bottom *h*-BN layers. Scale bar, 10 µm. (d) SEM image of the PC waveguide with two air-slots. Scale bar, 1 µm. (e) Simulated electric field distributions of the guided mode in the PC waveguide integrated with the *h*-BN and $MoTe_2$ layers shown in the in-plane (top) and cross sectional (bottom) views. The $MoTe_2$ layer couples with the evanescent field effectively. Scale bar, 0.5 µm (top) and 0.1 µm (bottom).

Electrically Controlled $MoTe_2$ *p-i-n* Homojunction. Electrical and optoelectronic measurements of the fabricated device are carried out at room temperature in ambient conditions. As reported in previous works, the $MoTe_2$ layer encapsulated by the top and bottom *h*-BN flakes is electrically ambipolar.[14, 17] By applying different gate voltages (V_{G1}, V_{G2}, refer to Figure 2a) via the two side sections of the air-slotted PC waveguide, the top $MoTe_2$ layer could be doped with different carrier types by the electrostatic fields, which is expected to constitute different types of homojunction. The boundaries of the *p-i-n* regions formed in the $MoTe_2$ layer are indicated in Figure 2a. For example, by setting $V_{G1} < 0$ ($V_{G2} > 0$), the left (right) region of the $MoTe_2$ channel is doped into *p*- (*n*-) type. Considering the ultrathin dielectric layer (33 nm thick *h*-BN), the vertical electric fields provided by the left and right gates have few effects on the central region of the $MoTe_2$ channel, which promises its intrinsic electronic property. The width of the intrinsic region is about 680 nm between the two air-slots of the PC waveguide, which is larger than the diffusion distances of the doped electrons and holes. The depletion region is mainly determined by the length of the intrinsic layer, which is usually larger than those of the space charge regions at the interfaces of the doped region and intrinsic region. As a result, a *p-i-n*

homojunction is formed. Compared with the *p-n* homojunction of 2D materials, the intrinsic region is expected to absorb more photons, so the built-in electric field across the whole intrinsic region can reliably improve the efficiency of photoelectric conversion. With other gating configurations, *n-i-p*, *n-i-n*, and *p-i-p* homojunctions could be realized as well.

Figure 2b displays the output characteristic (I_{ds}–V_{ds}) curves of the device when the gate configurations are set as (V_{G1} = –5 V, V_{G2} = 3 V) and (V_{G1} = 3 V, V_{G2} = –5 V), which correspond to the proposed *p-i-n* and *n-i-p* operation modes, respectively. Here, I_{ds} and V_{ds} are drain-source current and bias voltage. Strong rectifying behaviors are observed in both cases. The minuscule reverse saturation currents of ~87.5 pA and ~48.3 pA for *p-i-n* and *n-i-p* configurations are achieved, respectively. These ultralow turn-off currents could be ascribed to the long intrinsic region in the homojunction, which is preferable in photodetector applications. To better analyze the physical parameters of the $MoTe_2$ *p-i-n* and *n-i-p* homojunctions, we fit their forward current data on a semi-logarithmic scale with Shockley diode equation in terms of Lambert *W* function.[18, 19] The rapidly increased currents at the forward bias provide ideality factors of 1.2 and 1.0 for the *p-i-n* and *n-i-p* configurations, respectively. It indicates that the junction region is almost perfect, and the current transport process is mainly affected by carrier diffusion rather than recombination caused by defects.[20] These values indicate the high-quality lateral interface of the $MoTe_2$ *p-i-n* homojunction constructed on the bottom silicon PC waveguide with a simple and compact structure. It augers well for applications in chip-integrated high-performance optoelectronic devices, including photodetectors, modulators, and light-emitting diodes.

To comprehensively study the reconfigurability of the $MoTe_2$ homojunction integrated on the PC waveguide, we measure the gate voltage dependences of I_{ds} by varying V_{G1} and V_{G2} simultaneously. Figure 2c,d shows the absolute values of I_{ds} as functions of V_{G1} and V_{G2} for the

case of V_{ds} = 1.0 V and V_{ds} = –1.0 V, respectively. The four corners correspond to the *p-i-n*, *n-i-n*, *p-i-p*, *n-i-p* configurations of the conducting regions. The *p-i-n* and *n-i-p* homojunctions have obvious conducting and cut-off states in the forward and backward bias directions. On the contrary, there is no current cut-off in the *p-i-p* configuration when the bias is applied in both directions. It could be attributed to the same polarity over the left and right regions of the $MoTe_2$ channel and the slight *p*-doping in the central intrinsic region.[21] The barrier height formed by the concentration difference of holes at the interfaces of the doped region and intrinsic region is low, which is easy for carriers to pass through. Different from the case of *p-i-p* configuration, the *n-i-n* configuration is almost non-conductive in either forward or reverse bias. Since the central intrinsic region of the $MoTe_2$ channel is slightly *p*-doped, the *n-i-n* homojunction performs as a *n-p-n* homojunction, which has high junction barriers at the *n-i* and *i-n* interfaces. Neither electrons nor holes could easily pass through the junction barriers. This conclusion is confirmed by the photoresponse of the waveguide-integrated $MoTe_2$ *n-i-n* homojunction when light is coupled into the PC waveguide, see details in Supporting Note 3. With the excitation of the waveguiding mode, photocarriers fill the center intrinsic region, allowing the reduction of the barrier heights at the junction interfaces. Strong photocurrents are observed with a light on/off photoresponse ratio of 10^5. It also excludes the effect of the Schottky barrier height of Au–$MoTe_2$ on the I_{ds}–V_{ds} for different doping types. The light illumination on the $MoTe_2$ channel by the waveguiding mode is only applied over the central intrinsic region, which is far from the metal contacts. Hence, the variation of I_{ds} under dark condition and with light illumination is only determined by the photoresponse of the central intrinsic region. There is no optically induced effect over the Au–$MoTe_2$ regions. The specific results and analysis are seen in Supporting Note 3.

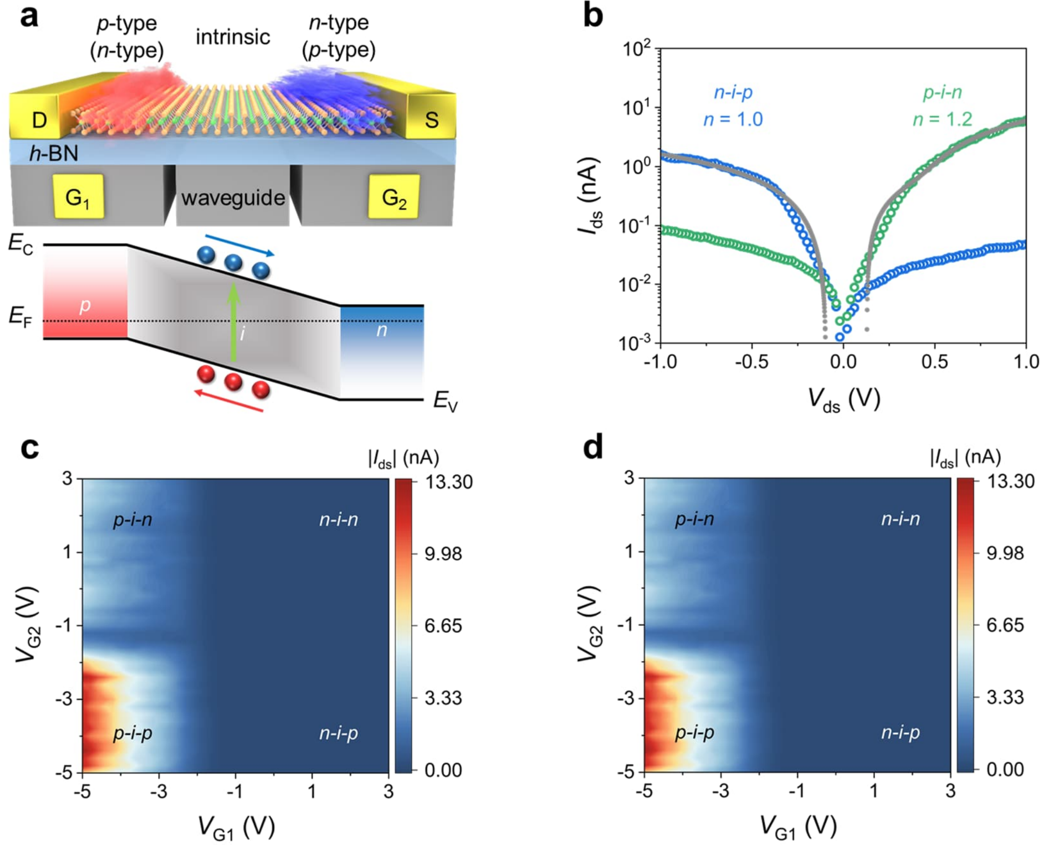

Figure 2. Electrically controlled $MoTe_2$ homojunction gated by the air-slotted PC waveguide. (a) Schematic of electrostatic doping on the few-layer $MoTe_2$ (upper panel) and energy band structure of lateral $MoTe_2$ *p-i-n* homojunction under the equilibrium state (lower panel). A negative (positive) gate potential causes the $MoTe_2$ layer to be doped in *p*-type (*n*-type). (b) Output curves (I_{ds}–V_{ds}) measured from *p-i-n* and *n-i-p* configurations of the $MoTe_2$ homojunction. The fitting curves give diode ideality factors of n = 1.2 and n = 1.0 for *p-i-n* and *n-i-p* configurations, respectively. (c, d) Current $|I_{ds}|$ as functions of split gate configurations at constant biases of (c) V_{ds} = 1.0 V and (d) V_{ds} = –1.0 V.

Photoresponses of Waveguide-integrated $MoTe_2$ *p-i-n* Homojunction. As well demonstrated in photodetectors of bulk materials, *p-i-n* junction is one of the best candidates to endow low dark current, high responsivity, and fast response speed. Similarly, the achieved

$MoTe_2$ *p-i-n* homojunction integrated on the PC waveguide is expected to support high-performance on-chip photodetections. To examine that, we couple light into the PC waveguide coated with the $MoTe_2$ homojunction via the grating coupler at the end of the waveguide, as shown in Figure 1c. A telecommunication O-band laser with a tunable wavelength range from 1260 nm to 1360 nm is used as the light source, as the light could be absorbed by the few-layer $MoTe_2$ due to its moderately small electronic bandgap.[22] Actuated by the built-in or external electric field laterally across the $MoTe_2$ homojunction, the generated photocarriers are separated and collected by the drain and source electrodes to yield a photocurrent, which is monitored with a high-precision electrical source-meter. To characterize the photoresponsivity, the optical absorption coefficient on the waveguiding mode by the few-layer $MoTe_2$ is determined to be ~0.55 dB/μm, as discussed in the Supporting Note 4.

With light coupled into the device, the short-circuit current I_{sc} (photocurrent without any external bias) and open-circuit voltage V_{oc} (photovoltage with no current flowing) are first measured with the $MoTe_2$ homojunction operating in different configurations, as shown in Figure 3a,b. The laser wavelength is set as λ = 1260 nm, and the optical power absorbed by the few-layer $MoTe_2$ is determined as P_{abs} = 65 μW. Referring to the (V_{G1}, V_{G2})-induced homojunction types shown in Figure 2c,d, large I_{sc} and V_{oc} are obtained in the regimes of *p-i-n* and *n-i-p* homojunctions, where the two gates are oppositely applied. In the *n-i-n* and *p-i-p* configurations, there is barely any measured signal. These results benefit from the photovoltaic effect with a large build-in electric field over the whole intrinsic region of the $MoTe_2$ channel, where most of the photocarriers are generated due to the effective overlap with the guided mode of the PC waveguide. The built-in electric field separates the photogenerated electrons (holes) to the drain (source) electrodes. For the *p-i-p* and *n-i-n* configurations (V_{G1} = V_{G2}), though there are

electric potentials at the interfaces between the doped region and intrinsic region, the built-in electric fields at the two interfaces have opposite directions, which cannot drive net photocarriers to the electrodes. The functions of I_{sc} and V_{oc} on the gate voltages are consistent with the magnitude of the rectification shown in Figure 2c,d. The maximum I_{sc} (V_{oc}) of 3.72 μA (0.45 V) is obtained from the *p-i-n* homojunction, indicating the high photoelectric conversion efficiency.

With a reverse bias on the $MoTe_2$ *p-i-n* homojunction, the electric field over the $MoTe_2$ channel could be strengthened compared to the internal built-in electric field. Also, as discussed above, the $MoTe_2$ *p-i-n* homojunction has an ultralow turn-off current under reverse bias. Hence, it is preferable to implement the photodetection in the $MoTe_2$ *p-i-n* homojunction with a reverse bias. By setting the waveguide-integrated $MoTe_2$ homojunction in the *p-i-n* configuration with $V_{G1} = -5$ V and $V_{G2} = 3$ V, we characterize its I_{ds}–V_{ds} curves without and with light coupled in the PC waveguide (at the wavelength of 1302 nm), as shown in Figure 3c. Compared with the dark condition, the I_{ds}–V_{ds} curves shift upwards greatly with the excitation of the guided mode, and the shift trend is proportional to the absorption powers by the $MoTe_2$ layer. Because the separated photocarriers cancel out the open-circuit voltage over the homojunction, the minimum I_{ds} is obtained with a positive V_{ds} of ~0.5 V.

We define the photocurrent as $I_{ph} = I_{ds,light} - I_{ds,dark}$ with $I_{ds,light}$ and $I_{ds,dark}$ as the I_{ds} measured with and without light coupled in the waveguide, respectively. Under the bias of $V_{ds} = -1.0$ V and the absorption power in the $MoTe_2$ layer as 9.80 μW, the generated photocurrent is 3.92 μA with a dark current of 87.5 pA. The photocurrent on/off ratio exceeds 10^4. Figure 3d plots the photocurrents measured with varied absorbed optical powers in the two cases of zero-bias and reverse bias with $V_{ds} = -1$ V. Both of them show linear dependence, which is determined by the linear photocarrier separation mechanism in the *p-i-n* configuration. The responsivity is

estimated as $R = I_{sc}/P_{abs}$=275 mA/W at zero-bias. The corresponding internal quantum efficiency (IQE) is calculated as IQE = $R\times(hc/q\lambda)$ =26.3%, where R, h, c, q, and λ are the responsivity, Planck's constant, speed of light, electron charge, and wavelength, respectively. The high responsivity and IQE with zero-bias are ascribed to the high quality of the *p-i-n* homojunction. Considering the moderately high photoresponsivity, the operation with zero-bias guarantees the on-chip self-powered photodetection with ultralow dark current and zero power consumption. By further increasing the gate voltages to strengthen the barrier height of the *p-i-n* homojunction, even higher responsivity could be achieved. The responsivity $R = I_{ph}/P_{abs}$ at the bias of $V_{ds} = -1.0$ V is estimated as 400 mA/W with a corresponding IQE of 38.2%. These improved performances are beneficial from the strengthened electric field across the junction by the reverse bias.

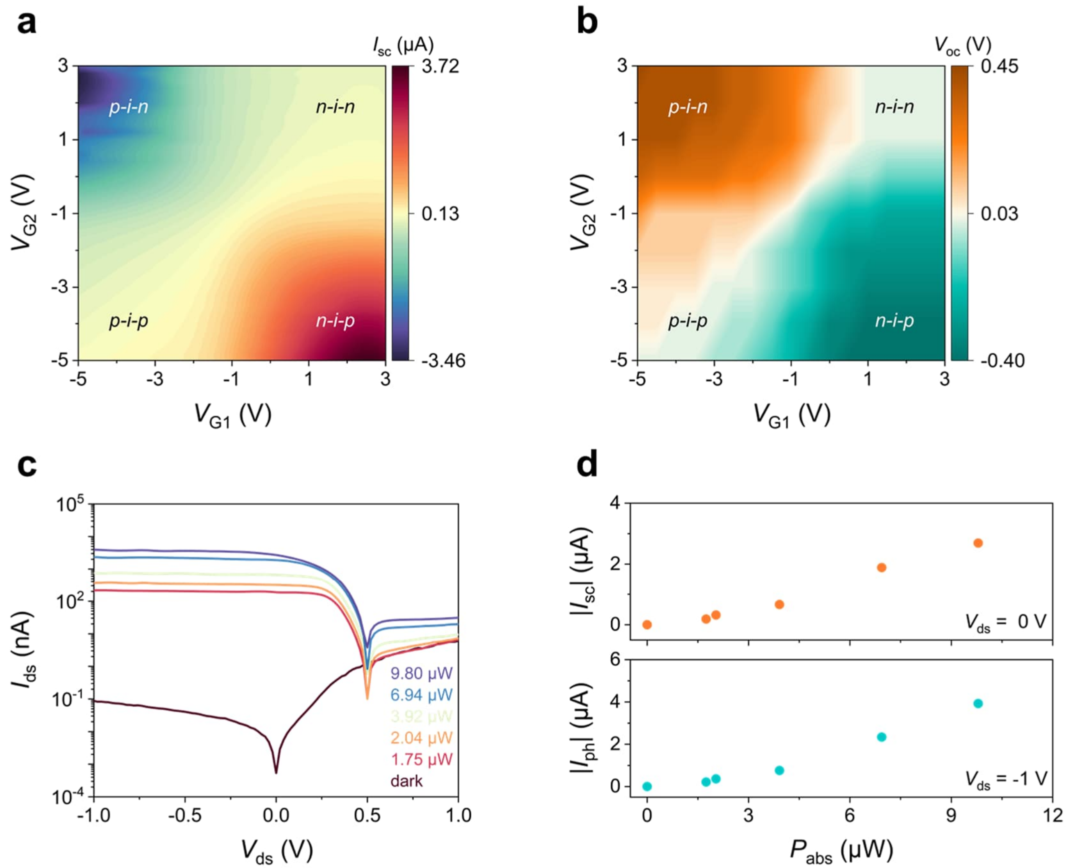

Figure 3. Photoresponses of $MoTe_2$ homojunctions integrated on silicon PC waveguide. (a, b) (a) Short-circuit current (I_{sc}, V_{ds} = 0 V) and (b) open-circuit voltage (V_{oc}, I_{ds} = 0 A) measured from the $MoTe_2$ homojunctions illuminated by the guided mode in the PC waveguide (λ = 1260 nm, P_{abs} = 65 µW). Gate voltages (V_{G1} and V_{G2}) are varied independently from –5 V to 3 V. (c) I_{ds}–V_{ds} curves in the $MoTe_2$ *p-i-n* homojunction (V_{G1} = −5 V, V_{G2} = 3 V) measured under the dark and with different absorption optical powers. (d) Power dependences of photocurrents at zero-bias and reverse bias of –1 V of the $MoTe_2$ *p-i-n* homojunction (V_{G1} = −5 V, V_{G2} = 3 V).

The few-layer $MoTe_2$ has an electronic bandgap around 0.93 eV, which cannot absorb the light over the whole telecommunication O-band. We evaluate the wavelength-dependent photoresponses of the waveguide-integrated $MoTe_2$ homojunction, as shown in Figure 4a. By tuning the wavelength of the laser coupled in the PC waveguide from 1260 nm to 1360 nm, the photocurrents of the $MoTe_2$ homojunction worked in the configuration of *p-i-n* (*n-i-p*) are measured with the bias voltages as 0 V and –1 V (0 V and 1 V). In the four cases, considerable photocurrents are obtained at the short wavelength range, though the values are much larger if external bias voltages are applied than those obtained with zero-bias. The photocurrents are cutoff around the wavelength of 1340 nm, which is determined by the absorption band of the few-layer $MoTe_2$. In the wavelength range between 1260 nm and 1320 nm, the photocurrents show an almost flat response, promising a broadband operation of the waveguide-integrated $MoTe_2$ homojunction photodetector in the O-band. Stronger photoresponses at the wavelength range shorter than 1260 nm are expected surely because few-layer $MoTe_2$ has larger optical absorption coefficient. For photodetection in a longer wavelength range than 1340 nm with the proposed waveguide-integrated $MoTe_2$ homojunction, a strategy of strained $MoTe_2$ could be exploited.[23]

The waveguide-integrated $MoTe_2$ *p-i-n* homojunction has an ultrasmall capacitance of 4.83×10^{-7} pF (see Supporting Note 6). As a result, the *RC* constant of the device would not limit the dynamic response speed of the photodetection. In addition, because the diffusion distance of photocarriers is smaller than the width of the middle intrinsic region of the $MoTe_2$ homojunction and the high-quality homojunctions have few defects, the carrier recombination lifetime would not limit the response speed either. The carrier transit time across the long $MoTe_2$ channel determines the final response speed, which is calculated as $\tau_{tr}=\frac{d}{2\upsilon}=\frac{d^2}{2\mu V_{sum}}$, where d is the width of the intrinsic region (680 nm), μ is the carrier mobility (value adopted from the literature[24]), V_{sum} is the sum of open circuit photovoltage (0.5 V) and bias voltage. The τ_{tr} is calculated to be 29.4 ps with a bias voltage of $V_{ds} = -1$ V, which corresponds to a dynamic response bandwidth of 34.0 GHz. More discussions are provided in Supporting Note 6. Unfortunately, due to the absence of instruments for measuring fast photoresponse, this high dynamic bandwidth cannot be presented in this work. We examine the ability of dynamic response on the waveguide-integrated $MoTe_2$ homojunction photodetector by modulating the laser power using its internal electro-optic modulator with a function generator. The time-dependent photocurrents are monitored by the source-meter, which has a limit of time resolution. Figure 4b displays the measurement results from a *p-i-n* homojunction biased at $V_{ds} = -1$ V with the illumination of 1260 nm light. The rise time (τ_{rise}) and fall time (τ_{fall}) are extracted from the times for the photocurrent rises from 10% to 90% and falls from 90% to 10% of the peak, which are τ_{rise} = 2.46 μs and τ_{fall} = 2.45 μs, respectively.

The normalized photocurrent-to-dark-current ratio (NPDR) is an important indicator to evaluate the photodetectivity of a chip-integrated photodetector,[25] which is expressed as NPDR = $(I_{ph}/I_{ds,dark})/P$, where P is the laser power coupled into the waveguide. The evaluated NPDRs of

the device in the *p-i-n* (*n-i-p*) configuration at different bias voltages are plotted in Figure 4c. With V_{ds} = –1 V (V_{ds} = 1 V), the NPDRs realized on the $MoTe_2$ *p-i-n* (*n-i-p*) homojunction photodetector are in the order of 10^6 mW^{-1}, which are further greatly improved to 10^7 mW^{-1} under the small bias voltage and reach a record-high value of 10^9 mW^{-1} (10^{10} mW^{-1}) at zero-bias. Even at the laser wavelength of 1340 nm, which is close to the band-edge of the few-layer $MoTe_2$, the NPDRs at a bias voltage of 1V (zero-bias) are still in the order of 10^5 mW^{-1} (10^8 mW^{-1}) though the absorption coefficient of $MoTe_2$ is very small. This performance transcends 2D material-based photodetectors[26-29] by several orders of magnitude and even exceeds typical Ge-based photodetectors.[30-32] The NPDR enhancement could be credited to the effective suppression of the dark current in the $MoTe_2$ *p-i-n* (*n-i-p*) homojunction without the sacrifice of the photocurrent. Under the same absolute value of opposite bias, the lower dark current of *n-i-p* homojunction compared to *p-i-n* homojunction leads to higher NPDR. The device is of great significance in high sensitivity and weak-light detection systems. To appraise the performance of the fabricated waveguide-integrated $MoTe_2$ *p-i-n* homojunction photodetector, Figure 4d compares the various waveguide-integrated and vertically free-space illuminated photodetectors on an NPDR/responsivity map (more types and indexes of the photodetectors are seen in Supporting Table 1). The device has a competitive photoresponse and NPDR for broad application giving high-performance on-chip photodetection. The performance could be further improved by choosing more suitable electrode material to reduce the contact resistance, optimizing the structure of PC waveguide for the appearance of slow light effect or extending the width of $MoTe_2$ to increase the light-matter interactions.

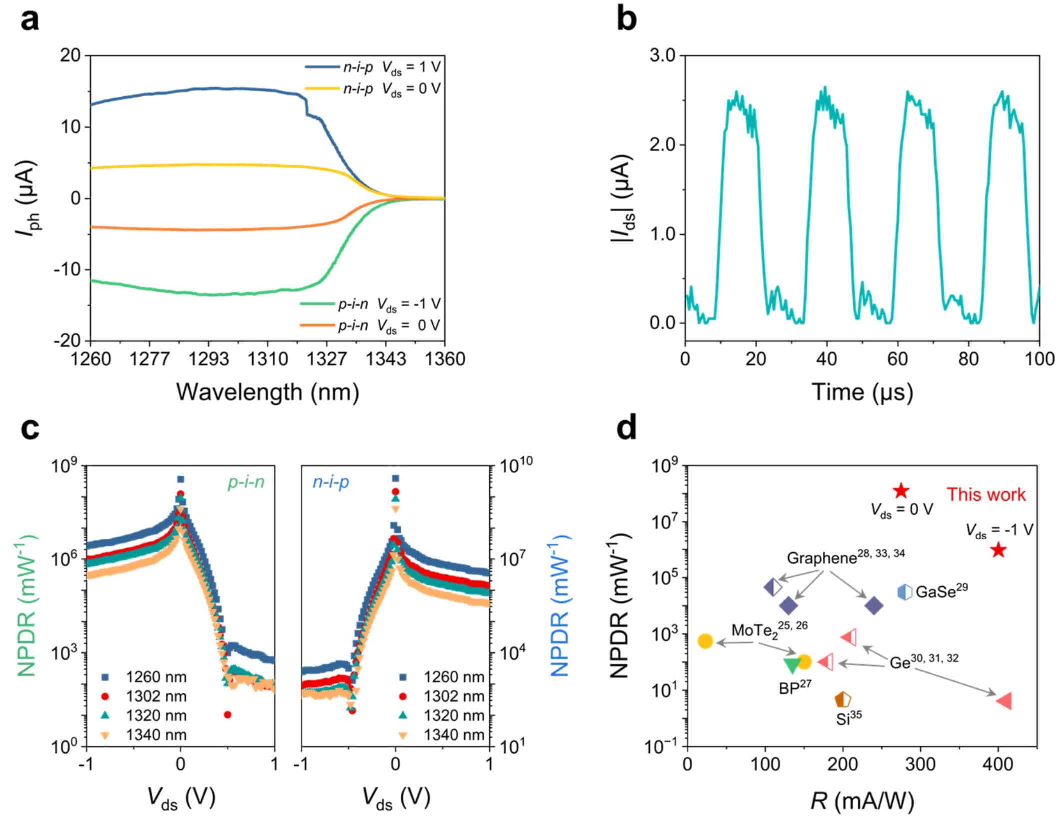

Figure 4. Performances of the waveguide-integrated $MoTe_2$ *p-i-n* homojunction photodetector. (a) Wavelength-dependent photocurrents of the waveguide-integrated $MoTe_2$ *p-i-n* and *n-i-p* homojunctions with and without bias. (b) Time-resolved photoresponse of the waveguide-integrated $MoTe_2$ *p-i-n* homojunctions at a bias of V_{ds} = –1 V. (c) NPDR as a function of applied bias voltages in the waveguide-integrated $MoTe_2$ *p-i-n* and *n-i-p* homojunctions. (d) Comparison of the responsivity and NPDR between the waveguide-integrated $MoTe_2$ *p-i-n* homojunction photodetector (with and without bias) and other waveguide-integrated and vertical illuminated photodetectors. The solid and the half-filled icons on the left represent the photodetectors integrated with waveguides or not, respectively. References: $MoTe_2$[25, 26], BP[27], graphene[28, 33, 34], GaSe[29], Ge[30-32] and Si[35].

CONCLUSION

Photodetectors integrated on silicon photonic chips were widely realized by heteroepitaxy or wafer-bonding of Ge or III-V compound semiconductors. Unfortunately, the integration processes of these bulk materials are complicated, and there are serious interface defects and impurities induced by the lattice mismatch with the silicon substrate, which inevitably results in a large dark current and hinders photocarrier separation. 2D materials, such as $MoTe_2$ employed in this work, have dangling-bond-free surfaces, enabling their hetero-integrations on silicon photonics with ideal interfaces to maintain their unique optical and electronic properties. Wafer-scale growth of highly crystalline $MoTe_2$ on silicon was demonstrated recently, showing high-quality intrinsic properties.[36] Though the mechanically exfoliated $MoTe_2$ is employed in this work, the developed wafer-scale $MoTe_2$ might support future large-scale manufacturing of the proposed device. In addition, different from *p*-*i*-*n* junctions in bulk materials requiring complicated selective ion-implantation and annealing, the waveguide-integrated $MoTe_2$ *p*-*i*-*n* homojunction could be realized easily with simple electrostatic doping using the back-gates fabricated on silicon PC waveguide. This homojunction is electrically reconfigurable with *p*-*i*-*n*, *n*-*i*-*p*, *n*-*i*-*n*, and *p*-*i*-*p* operations, which could be extensively exploited for on-chip optoelectronic logic functions. The device structure is simple, and the implementation is straightforward. Further, a non-volatile $MoTe_2$ *p*-*i*-*n* homojunction could be built on the PC waveguide by replacing the *h*-BN with a ferroelectric layer, such as HZO and PVDF.

The measured results of the fabricated waveguide-integrated $MoTe_2$ *p*-*i*-*n* homojunction indicate the high-quality rectification behavior with the ideality factors approaching 1.0 and ultralow turn-off current less than 90 pA. With the assistance of the extended light–$MoTe_2$ interaction provided by the guided mode of the PC waveguide, the telecommunication O-band

light could be absorbed by the $MoTe_2$ homojunction effectively, promising high-performance photodetection. The light on/off current ratio exceeds 10^4. A high photoresponsivity around 0.4 A/W is obtained over the wavelength range from 1260 nm to 1320 nm. Benefiting from the ultralow dark current of the *p-i-n* homojunction, a record-high NPDR of 10^6 mW^{-1} is achieved. The small capacitance of the $MoTe_2$ *p-i-n* homojunction also supports high dynamic response bandwidth close to 34.0 GHz. These realized merits are competitive compared with those of other waveguide-integrated photodetectors based on 2D materials and bulk materials. Besides the application in photodetectors, the silicon chip-integrated $MoTe_2$ homojunction could also be employed in other on-chip optoelectronic devices, such as electro-optic modulators, laser diodes, etc.

METHODS

Device Fabrication. The PC waveguide and electrical isolation air-slots were fabricated on a silicon-on-insulator (SOI) substrate. The patterns were designed together in the same layout, which were defined in a 400 nm thick AR-P 6200.13 resist layer using the electron beam lithography. The patterns were next etched by inductively coupled plasma. After the transfer of the patterns to the substrate, the resist was chemically removed using N-methyl-2-pyrrolidone and piranha solution. The $MoTe_2$ and *h*-BN layers were mechanically exfoliated and placed onto the surface of polydimethylsiloxane (PDMS), which were then dry transferred onto the PC waveguide with the assistance of a precise alignment system.[37, 38] The thickness were roughly identified by optical contrast, and then confirmed by AFM and Raman characterizations. Next, Au electrodes (with a thickness of 50 nm) were picked by PDMS and released accurately onto the $MoTe_2$ layer as the drain and source electrodes. A second *h*-BN flake was eventually

transferred on the top of the $MoTe_2$ channel to protect it from the environment. Finally, the device was annealed in an Ar/H_2 (95%/5%) atmosphere with a temperature of 473 K for 2 hours.

Electrical and Optoelectronic Measurements. Electrical and optoelectronic measurements of the fabricated waveguide-integrated $MoTe_2$ *p-i-n* homojunction were carried out with a semiconductor parameter analyzer (PDA FSpro) at room temperature in ambient conditions. Light from a tunable laser (TSL-510, Santec) was launched into an optical fiber and aligned to the input grating coupler of the PC waveguide with a six-axis micromanipulator. The transmission optical powers of the PC waveguide were monitored from the other grating coupler. The coupling efficiency of the PC waveguide and absorption power of the few-layer $MoTe_2$ were measured by the transmission spectrum at each step in the device preparation process (see Supporting Note 4 for details). The response time of the device was measured by the semiconductor parameter analyzer, and the modulation of the laser was realized using a function generator (AFG 3101, Tektronix) which created square wave pulses.

ASSOCIATED CONTENT

Supporting Information

The Supporting Information is available free of charge on the ACS Publications website at DOI: xxx.

S1, Raman and AFM characterizations of the 2D materials; S2, Structure design and mode simulation of the PC waveguide; S3, Analysis of electrical characteristics of the fabricated device; S4, Calculations of the absorption power; S5, Supporting results of responsivity and quantum efficiency of the device demonstrated in the maintext; S6, Estimation of the

response speed of the waveguide-integrated $MoTe_2$ *p*-*i*-*n* homojunction photodetector; S7, Performance comparisons with other waveguide-integrated and vertical illuminated photodetectors; S8, The stability of the device; S9, Another waveguide-integrated $MoTe_2$ *p*-*i*-*n* homojunction photodetector (PDF)

AUTHOR INFORMATION

Corresponding Author

Xuetao Gan — *Key Laboratory of Light Field Manipulation and Information Acquisition, Ministry of Industry and Information Technology, and Shaanxi Key Laboratory of Optical Information Technology, School of Physical Science and Technology, Northwestern Polytechnical University, Xi'an 710129, China;* orcid.org/0000-0003-2469-5807; E-mail: xuetaogan@nwpu.edu.cn

Authors

Chen Li — *Key Laboratory of Light Field Manipulation and Information Acquisition, Ministry of Industry and Information Technology, and Shaanxi Key Laboratory of Optical Information Technology, School of Physical Science and Technology, Northwestern Polytechnical University, Xi'an 710129, China;* orcid.org/0000-0001-6237-361X

Ruijuan Tian — *Key Laboratory of Light Field Manipulation and Information Acquisition, Ministry of Industry and Information Technology, and Shaanxi Key Laboratory of Optical Information Technology, School of Physical Science and Technology, Northwestern Polytechnical University, Xi'an 710129, China*

Xiaoqing Chen — *Key Laboratory of Light Field Manipulation and Information Acquisition, Ministry of Industry and Information Technology, and Shaanxi Key Laboratory of Optical Information Technology, School of Physical Science and Technology, Northwestern Polytechnical University, Xi'an 710129, China*

Linpeng Gu — *Key Laboratory of Light Field Manipulation and Information Acquisition, Ministry of Industry and Information Technology, and Shaanxi Key Laboratory of Optical Information Technology, School of Physical Science and Technology, Northwestern Polytechnical University, Xi'an 710129, China*

Zhengdong Luo — *Wide Bandgap Semiconductor Technology Disciplines State Key Laboratory, School of Microelectronics, Xidian University, Xi'an 710071, China*

Qiao Zhang — *Key Laboratory of Light Field Manipulation and Information Acquisition, Ministry of Industry and Information Technology, and Shaanxi Key Laboratory of Optical Information Technology, School of Physical Science and Technology, Northwestern Polytechnical University, Xi'an 710129, China*

Ruixuan Yi — *Key Laboratory of Light Field Manipulation and Information Acquisition, Ministry of Industry and Information Technology, and Shaanxi Key Laboratory of Optical Information Technology, School of Physical Science and Technology, Northwestern Polytechnical University, Xi'an 710129, China*

Zhiwen Li — *Key Laboratory of Light Field Manipulation and Information Acquisition, Ministry of Industry and Information Technology, and Shaanxi Key Laboratory of Optical Information Technology, School of Physical Science and Technology, Northwestern Polytechnical University, Xi'an 710129, China*

Biqiang Jiang — *Key Laboratory of Light Field Manipulation and Information Acquisition, Ministry of Industry and Information Technology, and Shaanxi Key Laboratory of Optical Information Technology, School of Physical Science and Technology, Northwestern Polytechnical University, Xi'an 710129, China*

Yan Liu — *Wide Bandgap Semiconductor Technology Disciplines State Key Laboratory, School of Microelectronics, Xidian University, Xi'an 710071, China*

Andres Castellanos-Gomez — *Materials Science Factory, Instituto de Ciencia de Materiales de Madrid (ICMM-CSIC), Madrid E-28049, Spain;* orcid.org/0000-0002-3384-3405

Soo Jin Chua — *Department of Electrical and Computer Engineering, National University of Singapore, 4 Engineering Drive 3, Singapore 117583, Singapore; LEES Program, Singapore-MIT Alliance for Research & Technology (SMART), 1 CREATE Way, #10-01 CREATE Tower, Singapore 138602, Singapore*

Xiaomu Wang — *School of Electronic Science and Engineering, Nanjing University, Nanjing 210093, China*

Zhipei Sun — *Department of Electronics and Nanoengineering and QTF Centre of Excellence, Aalto University, Aalto FI-00076, Finland;* orcid.org/0000-0002-9771-5293

Jianlin Zhao — *Key Laboratory of Light Field Manipulation and Information Acquisition, Ministry of Industry and Information Technology, and Shaanxi Key Laboratory of Optical Information Technology, School of Physical Science and Technology, Northwestern Polytechnical University, Xi'an 710129, China*

Complete contact information is available at:

https://pubs.acs.org/xxx

Author Contributions

The manuscript was written through contributions of all authors. All authors have given approval to the final version of the manuscript.

Notes

The authors declare no competing financial interest.

ACKNOWLEDGMENTS

This project was primarily supported by the National Key R&D Program of China (Grant Nos. 2018YFA0307200), the National Natural Science Foundation of China (Grant Nos. 91950119, 61905196, and 62090033), Key Research and Development Program in Shaanxi Province of

China (Grant Nos. 2020JZ-10), and the Fundamental Research Funds for the Central Universities (Grant Nos. 310201911cx032, 3102019JC008, and D5000210905). The authors also thank the Analytical & Testing Center of NPU for their assistance in device fabrication and characterizations.

REFERENCES

(1) Liu, C.; Guo, J.; Yu, L.; Li, J.; Zhang, M.; Li, H.; Shi, Y.; Dai, D. Silicon/2D-material photodetectors: from near-infrared to mid-infrared. *Light: Sci. Appl.* **2021**, *10*, 123.

(2) Youngblood, N.; Li, M. Integration of 2D materials on a silicon photonics platform for optoelectronics applications. *Nanophotonics* **2016**, *6*, 1205-1218.

(3) Guo, J.; Li, J.; Liu, C.; Yin, Y.; Wang, W.; Ni, Z.; Fu, Z.; Yu, H.; Xu, Y.; Shi, Y.; Ma, Y.; Gao, S.; Tong, L.; Dai, D. High-performance silicon-graphene hybrid plasmonic waveguide photodetectors beyond 1.55 μm. *Light: Sci Appl* **2020**, *9*, 29.

(4) Schuler, S.; Schall, D.; Neumaier, D.; Dobusch, L.; Bethge, O.; Schwarz, B.; Krall, M.; Mueller, T. Controlled Generation of a p-n Junction in a Waveguide Integrated Graphene Photodetector. *Nano Lett.* **2016**, *16*, 7107-7112.

(5) Schuler, S.; Schall, D.; Neumaier, D.; Schwarz, B.; Watanabe, K.; Taniguchi, T.; Mueller, T. Graphene Photodetector Integrated on a Photonic Crystal Defect Waveguide. *ACS Photonics* **2018**, *5*, 4758-4763.

(6) Schuler, S.; Muench, J. E.; Ruocco, A.; Balci, O.; Thourhout, D. V.; Sorianello, V.; Romagnoli, M.; Watanabe, K.; Taniguchi, T.; Goykhman, I.; Ferrari, A. C.; Mueller, T. High-responsivity graphene photodetectors integrated on silicon microring resonators. *Nat. Commun.* **2021**, *12*, 3733.

(7) Bie, Y. Q.; Grosso, G.; Heuck, M.; Furchi, M. M.; Cao, Y.; Zheng, J.; Bunandar, D.; Navarro-Moratalla, E.; Zhou, L.; Efetov, D. K.; Taniguchi, T.; Watanabe, K.; Kong, J.; Englund, D.; Jarillo-Herrero, P. A $MoTe_2$-based light-emitting diode and photodetector for silicon photonic integrated circuits. *Nat. Nanotechnol.* **2017**, *12*, 1124-1129.

(8) Muench, J. E.; Ruocco, A.; Giambra, M. A.; Miseikis, V.; Zhang, D.; Wang, J.; Watson, H. F. Y.; Park, G. C.; Akhavan, S.; Sorianello, V.; Midrio, M.; Tomadin, A.; Coletti, C.; Romagnoli, M.; Ferrari, A. C.; Goykhman, I. Waveguide-Integrated, Plasmonic Enhanced Graphene Photodetectors. *Nano Lett.* **2019**, *19*, 7632-7644.

(9) Tian, R.; Gan, X.; Li, C.; Chen, X.; Hu, S.; Gu, L.; Van Thourhout, D.; Castellanos-Gomez, A.; Sun, Z.; Zhao, J. Chip-integrated van der Waals PN heterojunction photodetector with low dark current and high responsivity. *Light: Sci. Appl.* **2022**, *11*, 101.

(10) Wang, F.; Pei, K.; Li, Y.; Li, H.; Zhai, T. 2D Homojunctions for Electronics and Optoelectronics. *Adv. Mater.* **2021**, *33*, 2005303.

(11) Li, C.; Tian, R.; Yi, R.; Hu, S.; Chen, Y.; Yuan, Q.; Zhang, X.; Liu, Y.; Hao, Y.; Gan, X.; Zhao, J. $MoTe_2$ PN Homojunction Constructed on a Silicon Photonic Crystal Cavity for High-Performance Photodetector. *ACS Photonics* **2021**, *8*, 2431-2439.

(12) Tian, R. J.; Gu, L. P.; Ji, Y. K.; Li, C.; Chen, Y. X.; Hu, S. Q.; Li, Z. W.; Gan, X. T.; Zhao, J. L. Black Phosphorus Photodetector Enhanced by a Planar Photonic Crystal Cavity. *ACS Photonics* **2021**, *8*, 3104-3110.

(13) Xu, J.; Luo, X.; Hu, S.; Zhang, X.; Mei, D.; Liu, F.; Han, N.; Liu, D.; Gan, X.; Cheng, Y.; Huang, W. Tunable Linearity of High-Performance Vertical Dual-Gate vdW Phototransistors. *Adv. Mater.* **2021**, *33*, 2008080.

(14) Hu, S.; Xu, J.; Zhao, Q.; Luo, X.; Zhang, X.; Wang, T.; Jie, W.; Cheng, Y.; Frisenda, R.; Castellanos-Gomez, A.; Gan, X. Gate-Switchable Photovoltaic Effect in BP/$MoTe_2$ van der Waals Heterojunctions for Self-Driven Logic Optoelectronics. *Adv. Opt. Mater.* **2020**, *9*, 2001802.

(15) Hu, S.; Zhang, Q.; Luo, X.; Zhang, X.; Wang, T.; Cheng, Y.; Jie, W.; Zhao, J.; Mei, T.; Gan, X. Au-InSe van der Waals Schottky junctions with ultralow reverse current and high photosensitivity. *Nanoscale* **2020**, *12*, 4094-4100.

(16) Hu, S.; Tian, R.; Luo, X.; Yin, R.; Cheng, Y.; Zhao, J.; Wang, X.; Gan, X. Photovoltaic effects in reconfigurable heterostructured black phosphorus transistors. *Chin. Phys. B* **2018**, *27*, 128502.

(17) Larentis, S.; Fallahazad, B.; Movva, H. C. P.; Kim, K.; Rai, A.; Taniguchi, T.; Watanabe, K.; Banerjee, S. K.; Tutuc, E. Reconfigurable Complementary Monolayer $MoTe_2$ Field-Effect Transistors for Integrated Circuits. *ACS Nano* **2017**, *11*, 4832-4839.

(18) Baugher, B. W.; Churchill, H. O.; Yang, Y.; Jarillo-Herrero, P. Optoelectronic devices based on electrically tunable p-n diodes in a monolayer dichalcogenide. *Nat. Nanotechnol.* **2014**, *9*, 262-267.

(19) Banwell, T. C.; Jayakumar, A. Exact analytical solution for current flow through diode with series resistance. *Electron. Lett.* **2000**, *36*, 291-292.

(20) Zhang, Y.; Ma, K.; Zhao, C.; Hong, W.; Nie, C.; Qiu, Z. J.; Wang, S. An Ultrafast WSe_2 Photodiode Based on a Lateral *p-i-n* Homojunction. *ACS Nano* **2021**, *15*, 4405-4415.

(21) Fathipour, S.; Ma, N.; Hwang, W. S.; Protasenko, V.; Vishwanath, S.; Xing, H. G.; Xu, H.; Jena, D.; Appenzeller, J.; Seabaugh, A. Exfoliated multilayer $MoTe_2$ field-effect transistors. *Appl. Phys. Lett.* **2014**, *105*, 192101.

(22) Ruppert, C.; Aslan, O. B.; Heinz, T. F. Optical properties and band gap of single- and few-layer $MoTe_2$ crystals. *Nano Lett.* **2014**, *14*, 6231-6236.

(23) Maiti, R.; Patil, C.; Saadi, M. A. S. R.; Xie, T.; Azadani, J. G.; Uluutku, B.; Amin, R.; Briggs, A. F.; Miscuglio, M.; Van Thourhout, D.; Solares, S. D.; Low, T.; Agarwal, R.; Bank, S. R.; Sorger, V. J. Strain-engineered high-responsivity $MoTe_2$ photodetector for silicon photonic integrated circuits. *Nat. Photonics* **2020**, *14*, 578-584.

(24) Liu, X.; Islam, A.; Guo, J.; Feng, P. X. Controlling Polarity of $MoTe_2$ Transistors for Monolithic Complementary Logic via Schottky Contact Engineering. *ACS Nano* **2020**, *14*, 1457-1467.

(25) Ma, P.; Flöry, N.; Salamin, Y.; Baeuerle, B.; Emboras, A.; Josten, A.; Taniguchi, T.; Watanabe, K.; Novotny, L.; Leuthold, J. Fast $MoTe_2$ Waveguide Photodetector with High Sensitivity at Telecommunication Wavelengths. *ACS Photonics* **2018**, *5*, 1846-1852.

(26) Flory, N.; Ma, P.; Salamin, Y.; Emboras, A.; Taniguchi, T.; Watanabe, K.; Leuthold, J.; Novotny, L. Waveguide-integrated van der Waals heterostructure photodetector at telecom wavelengths with high speed and high responsivity. *Nat. Nanotechnol.* **2020**, *15*, 118-124.

(27) Youngblood, N.; Chen, C.; Koester, S. J.; Li, M. Waveguide-integrated black phosphorus photodetector with high responsivity and low dark current. *Nat. Photonics* **2015**, *9*, 247-252.

(28) Gao, Y.; Zhou, G.; Tsang, H. K.; Shu, C. High-speed van der Waals heterostructure tunneling photodiodes integrated on silicon nitride waveguides. *Optica* **2019**, *6*, 514-517.

(29) Hussain, M.; Aftab, S.; Jaffery, S. H. A.; Ali, A.; Hussain, S.; Cong, D. N.; Akhtar, R.; Seo, Y.; Eom, J.; Gautam, P.; Noh, H.; Jung, J. Asymmetric electrode incorporated 2D GeSe for self-biased and efficient photodetection. *Sci Rep* **2020**, *10*, 9374.

(30) Chi On, C.; Okyay, A. K.; Saraswat, K. C. Effective dark current suppression with asymmetric MSM photodetectors in Group IV semiconductors. *IEEE Photonics Technol. Lett.* **2003**, *15*, 1585-1587.

(31) Assefa, S.; Xia, F. N.; Bedell, S. W.; Zhang, Y.; Topuria, T.; Rice, P. M.; Vlasov, Y. A. CMOS-integrated high-speed MSM germanium waveguide photodetector. *Opt. Express* **2010**, *18*, 4986-4999.

(32) Zang, H. J.; Kim, G. S.; Park, G. J.; Choi, Y. S.; Yu, H. Y. Asymmetrically contacted germanium photodiode using a metal-interlayer-semiconductor-metal structure for extremely large dark current suppression. *Opt. Lett.* **2016**, *41*, 3686-3689.

(33) Wang, X.; Cheng, Z.; Xu, K.; Tsang, H. K.; Xu, J.-B. High-responsivity graphene/silicon-heterostructure waveguide photodetectors. *Nat. Photonics* **2013**, *7*, 888-891.

(34) An, Y.; Behnam, A.; Pop, E.; Ural, A. Metal-semiconductor-metal photodetectors based on graphene/p-type silicon Schottky junctions. *Appl. Phys. Lett.* **2013**, *102*, 013110.

(35) Okyay, A. K.; Chui, C. O.; Saraswat, K. C. Leakage suppression by asymmetric area electrodes in metal-semiconductor-metal photodetectors. *Appl. Phys. Lett.* **2006**, *88*, 063506.

(36) Xu, X.; Pan, Y.; Liu, S.; Han, B.; Gu, P.; Li, S.; Xu, W.; Peng, Y.; Han, Z.; Chen, J.; Gao, P.; Ye, Y. Seeded 2D epitaxy of large-area single-crystal films of the van der Waals semiconductor 2H $MoTe_2$. *Science* **2021**, *372*, 195-200.

(37) Meitl, M. A.; Zhu, Z.-T.; Kumar, V.; Lee, K. J.; Feng, X.; Huang, Y. Y.; Adesida, I.; Nuzzo, R. G.; Rogers, J. A. Transfer printing by kinetic control of adhesion to an elastomeric stamp. *Nat. Mater.* **2005**, *5*, 33-38.

(38) Castellanos-Gomez, A.; Buscema, M.; Molenaar, R.; Singh, V.; Janssen, L.; van der Zant, H. S. J.; Steele, G. A. Deterministic transfer of two-dimensional materials by all-dry viscoelastic stamping. *2D Mater.* **2014**, *1*, 011002.

For Table of Contents Use Only